Mutual coherent structures for heat and angular momentum transport in turbulent Taylor-Couette flows

X.-Y. Leng and J.-Q. Zhong[*]

School of Physics Science and Engineering, Tongji University, 200092 Shanghai, People's Republic of China

In this paper, we report numerical results of turbulent transport of heat Nu and angular momentum ν_t/ν in Taylor-Couette (TC) flows subjected to a radial temperature gradient. Direct numerical simulations are performed in a TC cell with a radius ratio $\eta = 0.5$ and an aspect ratio $\Gamma = 8$ for two Rayleigh numbers (Ra $= 10^5$, 10^6) and two Prandtl numbers (Pr $= 0.7$, 4.38), while the Reynolds number Re varies in the range of $0 \leqslant \text{Re} \leqslant 15\,000$. With increasing Re, the flows undergo evolution of different flow states: a first transition being from the convection-dominated regime to the transitional regime, with the large-scale meridional circulation evolving into spiral vortices; a second flow evolution occurring in the rotation-dominated regime when Taylor vortices turn from a weakly nonlinear state into a turbulent state. In particular, when the flows are governed by turbulent Taylor vortices, we find that both transport processes exhibit power-law scaling: $\text{Nu} \sim \text{Re}^{0.619\pm0.015}$ for Pr $= 4.38$, $\text{Nu} \sim \text{Re}^{0.590\pm0.025}$ for Pr $= 0.7$ and $\nu_t/\nu \sim \text{Re}^{0.588\pm0.036}$ for both Pr. These scaling exponents suggest an analogous mechanism for the radial transport of heat and angular momentum, which is further evidenced by the fact that the ratio of effective viscosity to diffusivity is independent of Re. To illustrate the underlying mechanism of turbulent transport, we extract the coherent structures by analyzing the spatial distributions of heat and momentum flux densities. Our results reveal mutual turbulent structures through which both heat and angular momentum are transported efficiently.

I. INTRODUCTION

Turbulent transport processes of heat, mass, and momentum are the central aspects in studying turbulence, owing to their close relations to various natural flows [1–5]. To understand the mechanism of turbulent transport is a challenging task in fluid physics and crucial for the related applications. Taylor-Couette (TC) flow, a fluid layer driven by two concentrically rotating cylinders, is of fundamental interest in many perspectives [4,6], for example, in probing the angular momentum transport in accretion disks [7–9]. It is also relevant to various applications in industry such as drag reduction [10,11] and solidification [12,13].

In TC flows, the toroidal motion of a Taylor vortex (TV) may enhance the mixing and transport efficiency. Hence, TC reactors are extensively applied to chemical, food, and biology processes [14–16]. In these applications, a heated or cooled cylinder is inevitable. It is thus desirable to investigate the flow structures and transport properties in the TC systems subjected to a radial temperature gradient. For modest Reynolds number (Re), studies of flow regimes, instabilities, and pattern formations in such TC systems have attracted a lot of attention, including experiments [17–22], stability analyses [23–26], and numerical simulations [27–30]. However, in turbulent TC flows, much less effort has been made to investigate the complex problem of the

---

*jinqiang@tongji.edu.cn

043501-1

turbulent transport processes, which are supposed to be more relevant to most applications in geophysical and industrial flows [8–10]. To better understand the relationships between the scalar and momentum transport in a high-Re regime, it is crucial to predict the interior structures and states of the flows. Furthermore, determination of the scaling laws of heat and momentum transport is vital to extrapolate the existing results from laboratories to large-scale geo- and astrophysical flows. It remains a challenging question to date whether the scalar and momentum transport by TC flows share similar scaling behaviors in the turbulent regime [31–33].

Coherent structures play an important role in turbulent transport processes [3]. In turbulent TC flows, the momentum transport is implemented by the coherent structures in forms of turbulent TVs and turbulent plumes between adjacent TVs [34–36]. The meridional advection of TVs sweeps the radial and axial boundaries simultaneously, potentially providing a similar transport mechanism in both directions. Indeed, in recent simulations [33], we find that when an axial temperature gradient is applied in turbulent TC flows, the axial heat-transport scaling is analogous to that of the radial transport of angular momentum [33]. This result confirms the existence of analogy between the axial dispersion of a passive scalar and the radial transport of momentum [31,32]. In the scenario that a radial temperature difference is applied in TC systems, both heat and angular momentum can be transported radially. In this system, how the large-scale structures, such as TVs, affect the turbulent transport processes is a natural question of great interest.

In this paper, we utilize the paradigmatic model of TC systems consisting of a heating (cooling) inner (outer) cylinder with two adiabatic end walls. We consider the radial transport processes of angular momentum and heat in a high-Reynolds-number regime. The results suggest that, in the regime of turbulent TVs, the radial transport of heat and angular momentum possess similar scaling relationships. Furthermore, by extracting fluid domains of high flux densities, we demonstrate that the heat and momentum transport are manipulated mainly by similar turbulent structures.

II. NUMERICAL SIMULATIONS

A. Physical model

We investigate the three-dimensional flow of an incompressible viscous fluid contained between two concentric cylinders of radii r_1, r_2, and height h. The inner wall is rotating about the z axis (e_z) with angular velocity ω_1, while the outer one is set to be fixed. A radial temperature difference Δ is imposed on the cylinders with the hot inner (t_1) and cold outer (t_2) walls. The fluid properties including kinematic viscosity ν, thermal expansion coefficient β, and thermal diffusivity κ are assumed to be constant. The governing parameters are the Rayleigh number $\mathrm{Ra} = \beta g \Delta d^3/(\nu \kappa)$, the Prandtl number $\mathrm{Pr} = \nu/\kappa$, and the Reynolds number $\mathrm{Re} = \omega_1 r_1 d/\nu$, respectively, where $d = r_2 - r_1$ is the gap width and g is the gravitational acceleration. The Richardson number $\mathrm{Ri} = \mathrm{Ra}/\mathrm{Pr}/\mathrm{Re}^2$, defined as the ratio of the free fall velocity to the inner-wall velocity, is adopted here to measure the relative strength between thermal convection and TC flow. Two important geometrical parameters entering into the problem are the aspect ratio $\Gamma = h/d$ and the radius ratio $\eta = r_1/r_2$. The gap width d, imposed temperature difference Δ, and inner-wall velocity $u_1 = \omega_1 r_1$ are introduced as the length, temperature, and velocity scales. Therefore, within the Boussinesq approximation, the dimensionless Navier-Stokes equations are

$$\frac{\partial \mathbf{U}}{\partial \tau} + (\mathbf{U} \cdot \boldsymbol{\nabla})\mathbf{U} = -\boldsymbol{\nabla} p + \frac{1}{\mathrm{Re}}\nabla^2 \mathbf{U} + \mathrm{Ri}Te_z, \quad \boldsymbol{\nabla} \cdot \mathbf{U} = 0, \tag{1}$$

$$\frac{\partial T}{\partial \tau} + (\mathbf{U} \cdot \boldsymbol{\nabla})T = \frac{1}{\mathrm{RePr}}\nabla^2 T, \tag{2}$$

where τ, p, and T are, correspondingly, time, pressure, and temperature. And $\mathbf{U}$ (U_r, U_θ, U_z) are the components of velocity in radial, azimuthal, and axial directions for cylindrical coordinates

TABLE I. A summary of the transitional values Re_1^* (Ri_1^*) and Re_2^* (Ri_2^*).

	Re_1^* (Ri_1^*)	Re_2^* (Ri_2^*)
$\mathrm{Ra} = 10^5$, $\mathrm{Pr} = 0.7$	500 (0.57)	2000(0.036)
$\mathrm{Ra} = 10^5$, $\mathrm{Pr} = 4.38$	150 (1.01)	2000(0.006)
$\mathrm{Ra} = 10^6$, $\mathrm{Pr} = 0.7$	1000(1.43)	4000(0.089)
$\mathrm{Ra} = 10^6$, $\mathrm{Pr} = 4.38$	300 (2.54)	2000(0.057)

(R, Θ, Z), respectively. The lower case letters t, $\mathbf{u}$ (u_r, u_θ, u_z), and (r, θ, z) denote the dimensional temperature, velocity, and coordinates. The dimensionless fluid angular velocity is ω. It is demonstrated in Appendix A that the effect of centrifugal buoyancy [26,28] does not change the main results and is thus neglected. The inner and outer cylinders are maintained at fixed temperatures $T_1 = 1$ and $T_2 = 0$, respectively, while end walls are set to be thermally insulating. No-slip boundaries are applied for velocities at all walls. We use a wide gap with the radius ratio $\eta = r_1/r_2 = 0.5$, and the aspect ratio is $\Gamma = h/d = 8$. This small-η system has been discussed widely by numerical simulations [37] and experiments [35,38].

Heat and angular momentum are two important transport quantities in the present system. In general, the global heat and angular momentum transport are expressed by Nu [39] and Nu$_\omega$ [40], respectively. The Nusselt number is defined as $\mathrm{Nu} = a^{-1}(\mathrm{RePr}\langle U_r T\rangle_V - \partial_r \langle T\rangle_V)$, where $\langle\rangle_V$ denotes the volume- and time-averaging and the geometry factor $a = 2d^2/[\ln(r_2/r_1)(r_2^2 - r_1^2)]$ is induced by the annular gap (see Appendix B). However, owing to the braking effect of the fixed end walls, Nu$_\omega$ decreases along the radial direction in our system [33]. As introduced in Appendix B, we use the dimensionless effective viscosity $\nu_t/\nu = (2\mathrm{Re}_\tau)^2/\mathrm{Re}$ to represent the angular momentum transport instead of Nu$_\omega$. Here, $\mathrm{Re}_\tau = 0.5u_\tau d/\nu$ is the friction Reynolds number with the friction velocity $u_\tau^2 = -\nu r(\partial\langle u_\theta/r\rangle_{\theta z}/\partial r)$ at the inner wall, where $\langle\rangle_{\theta z}$ denotes the azimuthal-, axial-, and time-averaging.

B. Numerical method

The equation system is solved using the finite difference scheme developed in Ref. [41] and modified for the cylindrical coordinate [33,42,43]. The numerical scheme is a second-order approximation based on the spatial discretization, which is nearly fully conservative with regard to mass, momentum, and kinetic energy. The second-order explicit Adams–Bashforth/backward-differentiation scheme is employed for the time discretization. The viscous terms are treated explicitly, and implicit treatment is applied for the diffusion term. At every time step, two Poisson equations, the projection method equation for pressure and the equation for temperature, are solved using fast-Fourier transforms in the azimuthal direction and the cyclic reduction direct solver [44]. Toward the walls, the clustered grid is implemented using the hyperbolic tangent coordinate transformation.

The grid sensitivity studies as well as the main results are listed in Tables II–IV in Appendix A. For each set of Ra, results from previous low-Re convections are used as the initial condition for the following high-Re case. Data from initial transient state are excluded, and data taken over a statistically steady state are averaged to determine the heat and angular momentum transport. The time convergence is checked by comparing the time averages over the whole and last halves of the simulation, and the resulting discrepancy is less than 3%. For the temporal resolution, the chosen time step $\Delta\tau$ satisfies the Courant-Friedrichs-Lewy (CFL) condition and the CFL number remains less than 0.5. The total run time for each case (including the initial and the averaging stages) is greater than 200 large eddy turnover time units, and the averaging time is not less than 100 large eddy turnover time units.
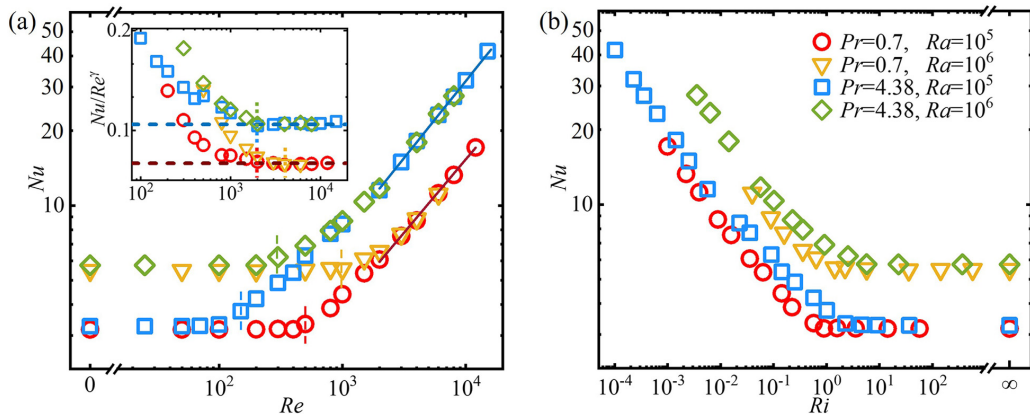
FIG. 1. (a) Global heat transport Nu as a function of Re for $Pr = 0.7$ and 4.38. Symbols are defined in panel (b). Solid lines denote the power-law fitting $Nu = \alpha Re^{\gamma}$ with $\gamma = 0.619$ for $Pr = 4.38$ (blue) and $\gamma = 0.590$ for $Pr = 0.7$ (red). Vertical dashed lines denote the first transition Re_1^*. Inset: An expanded view of the compensated plot of Nu as a function of Re. Vertical dotted lines denote the second transition Re_2^*. Dashed auxiliary lines indicate the values for the prefactor $\alpha = Nu/Re^{\gamma} = 0.106$ with $\gamma = 0.619$ (blue) and $\alpha = 0.068$ with $\gamma = 0.590$ (red). (b) Nu as a function of Ri.

III. RESULTS AND DISCUSSIONS

A. Global transport of heat and angular momentum

1. Radial heat transport

We first examine the global transport of heat. Data of the Nusselt number Nu are shown as a function of Re in Fig. 1(a) for $Ra = (10^5, 10^6)$ and $Pr = (0.7, 4.38)$. Without or with weak rotations ($0 \leqslant Re \leqslant 100$), the flow and heat transfer are dominated by vertical convection [45], and Nu is nearly independent of Re. We see that in this buoyancy-dominant flow regime, Nu is larger for a greater Ra for a given Re, but nearly independent of Pr. With increasing Re, Nu starts to grow when Re exceeds a critical value Re_1^* given in Table I. Interestingly, Nu for each Pr converges and becomes independent of Ra, indicating the fading away of buoyancy-driven convection. Further increasing Re, an obvious evolution of flow state takes place at Re_2^*, after which Nu exhibits a power-law scaling $Nu \sim Re^{\gamma}$ with $\gamma = 0.590 \pm 0.025$ for $Pr = 0.7$ and $\gamma = 0.619 \pm 0.015$ for $Pr = 4.38$ [see the compensated plot in the inset of Fig. 1(a)]. Both scalings for $Pr = 0.7$ and 4.38 suggest the existence of a new flow regime for heat transfer. All the transitional values Re_1^* and Re_2^* are listed in Table I. We find that at lower Pr or higher Ra, the more vigorously convective flows postpone the transitions.

We see in Fig. 1(a) the intriguing trend that in a TC system the radial heat transport Nu is insensitive to the variation of Pr in a low-Re flow regime ($Re < Re_1^*$), but becomes strongly dependent on Pr (independent of Ra) with sufficiently high Re. In the intermediate regime of Re, our data curves of Nu(Re) show complicated Ra and Pr dependence. To better clarify the variations of the heat transport with changing control parameters, we show in Fig. 1(b) the Nusselt number as a function of Richardson number Ri which measures the relative strength of buoyancy and rotation. In a high-Ri regime where the buoyancy-driven convection is dominant [corresponding to the low-Re regime shown in Fig. 1(a)], we see that Nu remains a constant. The first transition for Nu enhancement takes place at Ri_1^* that depends on both Ra and Pr. When $Ri \leqslant Ri_1^*(Ra, Pr)$, the strong rotations start to affect the flows and Nu increases monotonically as Ri decreases. With further decreasing $Ri \lesssim 1$, we find that Nu becomes larger for a greater Pr or Ra when Ri is given.
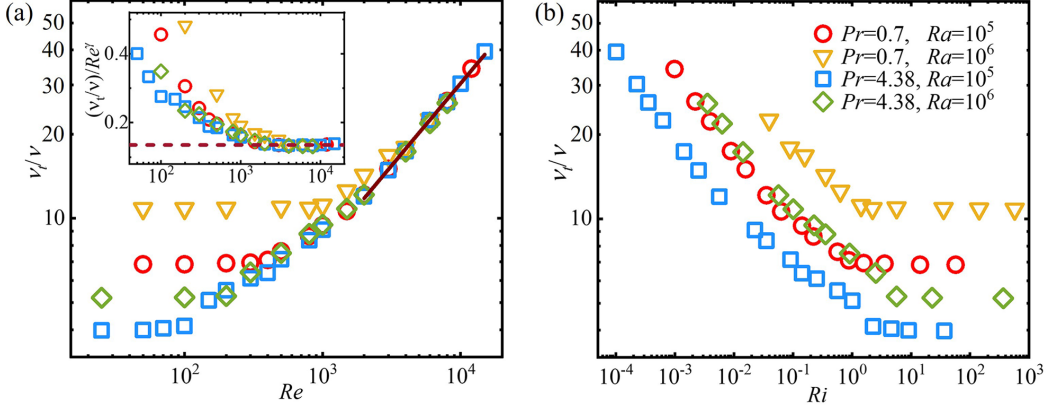
FIG. 2. (a) Dimensionless effective viscosity ν_t/ν as a function of Re for Pr = 0.7 and 4.38. Symbols are defined in panel (b). Solid line denotes the power-law fitting $\nu_t/\nu = \text{Re}^\gamma$ with $\gamma = 0.588$. Inset: An expanded view of the compensated plot of ν_t/ν as a function of Re. Dashed auxiliary line indicates the value for the prefactor $\alpha = (\nu_t/\nu)/\text{Re}^\gamma = 0.135$ with $\gamma = 0.588$. (b) ν_t/ν as a function of Ri.

2. Angular momentum transport

Figure 2(a) presents the dimensionless effective viscosity ν_t/ν as functions of Re for various Pr and Ra, which reveals the global angular momentum transport. In a low-Re regime where vigorous convection governs the flows, ν_t/ν is independent of Re but increases with a larger Ra or with a smaller Pr. Analogous to the heat transport data, we see that ν_t/ν starts to increase when Re exceeds the transitional value $\text{Re}_1^*(\text{Ra}, \text{Pr})$ obtained in Fig. 1(a). For various Ra and Pr, data of $\nu_t/\nu(\text{Re})$ converge to the same curve for Re > Re_1^*, and follow a unifying power-law scaling $\nu_t/\nu \sim \text{Re}^{0.588 \pm 0.036}$ after the evolution of flow state for Re > Re_2^* (see the compensated plot in inset). In Fig. 2(b), where the data are plotted as a function of Ri, we see that with decreasing Ri, ν_t/ν starts to increase at Ri_1^*. For very low Ri $\lesssim 1$, we find that ν_t/ν increases with increasing Ra, but decreases as Pr increases when Ri is given.

Further analyses are performed regarding the similar properties of heat and momentum transport for high Reynolds number. In Fig. 3, we show the ratio of the dimensionless effective viscosity ν_t/ν to the diffusivity κ_t/κ as a function of Re. The dimensionless effective diffusivity is defined as $\kappa_t/\kappa = a\text{Nu}$, where $a = 2d^2/[\ln(r_2/r_1)(r_2^2 - r_1^2)]$ is the geometry factor (Appendix B). It is found
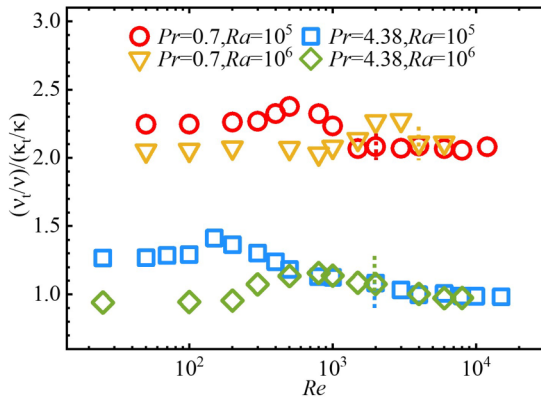

FIG. 3. The ratio of ν_t/ν over κ_t/κ as a function of Re. Vertical dotted lines denote Re_2^*.

that the ratio remains approximately a constant close to unity irrespective of Ra for Pr = 4.38 when Re > Re$_2^*$. The ratio appears larger for a lower Pr.

For each set of Ra and Pr, we have seen from above that the Reynolds-number dependencies of heat and angular momentum transport exhibit a similar trend. We argue that it is the evolution of the flow structures that governs the processes of both heat and angular momentum transport in the present system. In the following, we will gain some insights into the transport properties by analyzing the flow morphology and structures in different flow regimes.

B. Flow morphology

To illustrate the evolution of flow structures, we show two- and three-dimensional temperature fields in Fig. 4. Without rotations [Re = 0 as seen in Figs. 4(a) and 4(b)], the convective structure is axisymmetric, with a large-scale meridional circulation carrying ascending hot flows along the inner cylinder and descending cold flows along the outer cylinder. These are the typical temperature distributions in vertical convection [45–47]. For Re < Re$_1^*$, since the rotation is too weak to affect the circulation, we thus see that the Nu and ν_t/ν remain at their nonrotating values shown in Figs. 1 and 2. When the rotation effect becomes comparable to the buoyancy for Re $\geqslant$ Re$_1^*$, the flow undergoes the first transition from the meridional circulation to spiral vortices [see Figs. 4(c) and 4(d)], which starts to enhance the radial transport of heat and angular momentum. In this rotation-affected regime, we find that both the flow morphology and the transport properties are dependent on both Ra and Pr. With further increase in Re, rotation gradually dominates buoyancy, and the spiral vortices are replaced by the toroidal TVs [see Figs. 4(e) and 4(f)]. In this TC-dominated regime, Nu(Re) and ν_t/ν(Re) collapse, respectively, onto one curve that is independent of Ra [Figs. 1(a) and 2(a)]. The spiral vortices exist in an intermediate Ri-regime $0.089 \leqslant \text{Ri} \leqslant 2.54$ depending on Ra and Pr. In a similar system [48], the onset of spiral flow is reported in the range of $0.12 < \text{Ri} < 0.47$, showing a reasonable consistency with the present results. We note that the convection states of corotating and counterrotating vortices reported in Ref. [28] are not observed in the present study, presumably due to the different geometry of fluid domain used in the present study.

We see that with sufficiently large Reynolds number Re $\geqslant$ Re$_2^*$, the flow structure evolves into the turbulent TV flow [Figs. 4(g) and 4(h)], which is in good accord with previous studies in adiabatic TC systems [37] and in TC systems with a vertical temperature gradient applied [33]. In this flow regime, the turbulent transport of heat and momentum follows a unifying power-law scaling as shown in Figs. 1(a) and 2(a). In contrast to the flow fields with a lower Re (Re < Re$_2^*$), we can see that the temperature field with Re $\geqslant$ Re$_2^*$ consists of rich small-scale structures, with hot fluids pumped more efficiently into the bulk flow from the inner cylinder, resulting in a higher transport efficiency. Note that for Ra = 10^6 and Pr = 0.7, the vigorous buoyancy-driven turbulence largely postpones the evolution of flow state at Re$_2^*$. We thus find that the spiral vortices can persist for Re > 2000, and then turn into the turbulent TVs directly when Re > 4000.

C. Mutual coherent structures for heat and angular momentum transport

In this section, we demonstrate that mutual coherent structures in forms of turbulent TVs exist, through which both heat and angular momentum are transported efficiently in the high-Re flow regime. To verify this viewpoint, we present in Fig. 5 the flow fields and the spatial distributions of heat and angular velocity fluxes, respectively. In Fig. 5(a), three pairs of TVs characterize the time-averaged velocity field. The instantaneous temperature field shown in Fig. 5(b), however, is dominated by turbulent fluctuations. TVs can be recognized roughly as the hot (cold) plumes which are emanating from the inner (outer) cylinder toward the bulk flow. In the instantaneous fields of ω [Fig. 5(c)], we observe large-scale coherent structures, while TVs are hard to be identified. In Figs. 5(d) and 5(e), we further show the spatial distributions of convective flux densities of heat ($q_t^c/\langle q_t^c \rangle_V$) and angular velocity ($q_\omega^c/\langle q_\omega^c \rangle_V$), normalized by their averaged values (see definitions of flux densities in Appendix B). We can see that both the instantaneous flux densities exhibit a
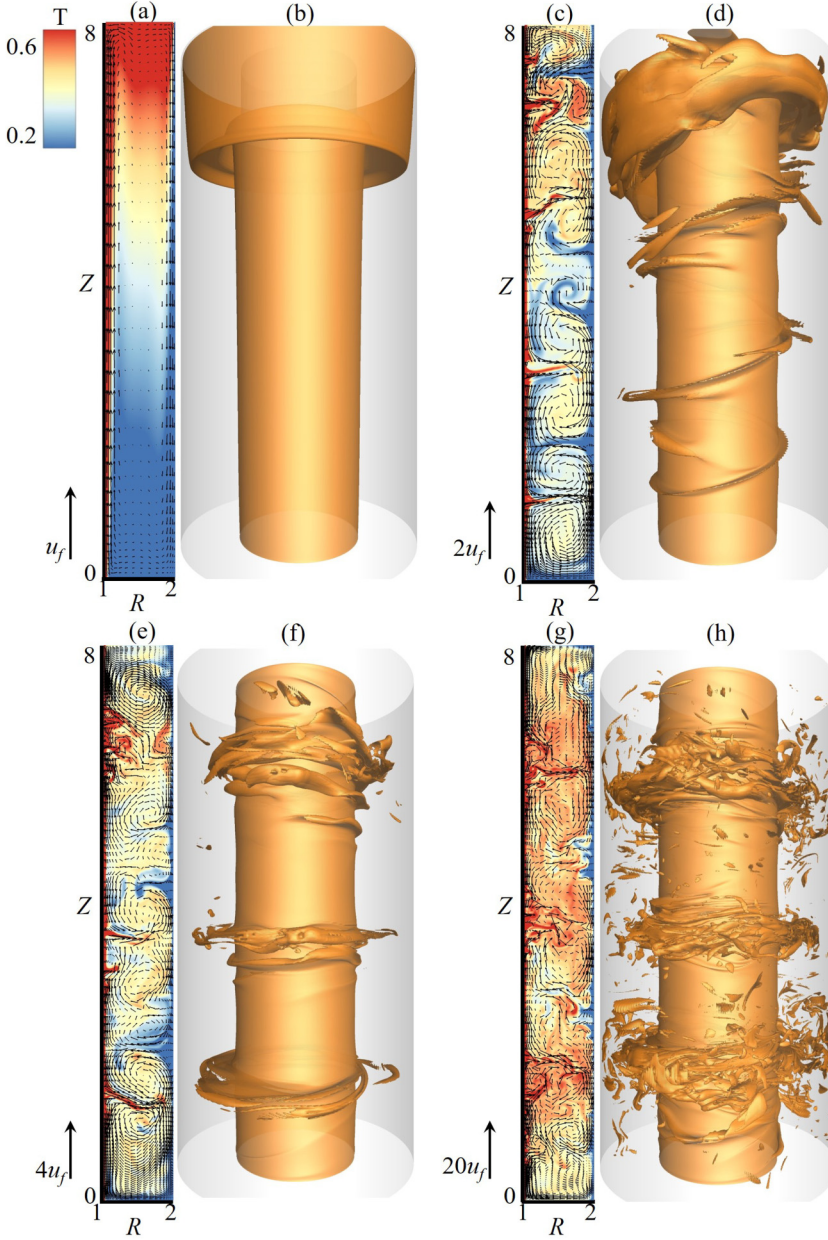
FIG. 4. Two-dimensional distributions of temperature and velocities in the meridional plane [(a), (c), (e), (g)] and three-dimensional temperature isosurfaces ($T = 0.52$) in the whole domain [(b), (d), (f), (h)] for Re= 0 [(a), (b)], 1000 [(c), (d)], 2000 [(e), (f)], and 4000 [(g), (h)] with Ra $= 10^6$ and Pr $= 4.38$. Vertical arrow on the left side of each panel denotes the velocity scale of free-fall velocity $u_f = \sqrt{\beta g \Delta d}$.

similar spatial distribution at any time. The plots of time-averaged flux densities of heat and angular velocity are given in Figs. 5(f) and 5(g), respectively. It is clear that the outward and inward jets of TVs govern the convective transport radially. Therefore, we conjecture that the turbulent heat and angular momentum transport are achieved through mutual coherent structures in forms of TVs in the high-Re regime.
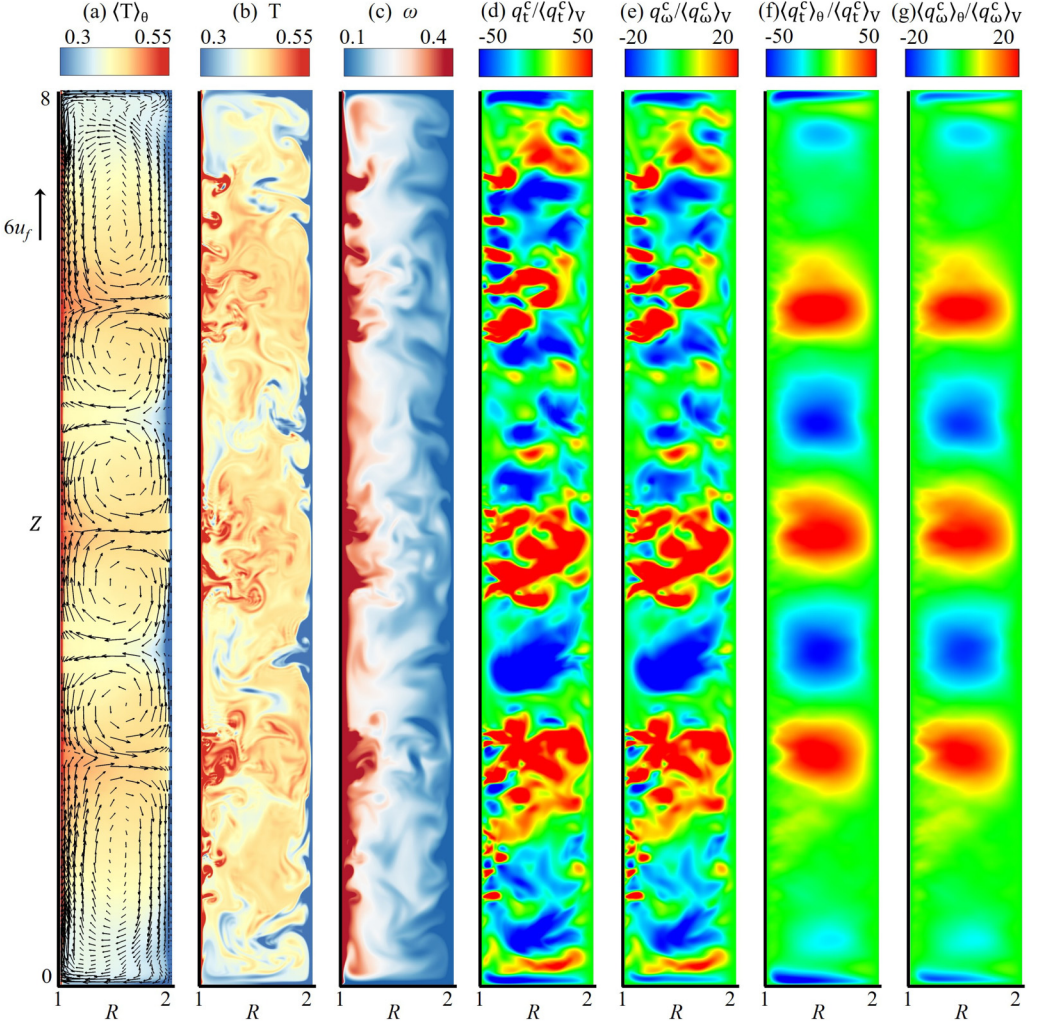
FIG. 5. Time-averaged velocity and temperature fields (a). Instantaneous distributions of fluid temperature T (b), angular velocity ω (c), the convective heat flux density $q_t^c/\langle q_t^c \rangle_V$ (d), and the convective angular velocity flux density $q_\omega^c/\langle q_\omega^c \rangle_V$ (e). Panels (a)–(e) are plotted in the same meridional plane. Time-averaged heat flux density $\langle q_t^c \rangle_\theta/\langle q_t^c \rangle_V$ and angular velocity flux density $\langle q_\omega^c \rangle_\theta/\langle q_\omega^c \rangle_V$ (g). For all panels $\mathrm{Re} = 6000$, $\mathrm{Ra} = 10^5$, and $\mathrm{Pr} = 4.38$. The arrow on the left of panel (a) denotes the velocity scale of free-fall velocity u_f. For comparisons, panels (d)–(g) are plotted using the same coloration.

To gain more insight into the mutual coherent structures for heat and angular momentum transport, we present data analysis of the spatial distribution of the local flux densities. We denote each spatial position of the fluid domain studied as $P(r, \theta, z)$. Following the strategy used in Refs. [49,50], we identify the pronounced structures of efficient turbulent transport, determining the spatial regions where the flux densities (q_t^c, q_ω^c) are greater than their averaged values $(\langle q_t^c \rangle_V, \langle q_\omega^c \rangle_V)$. Thus, for heat transport we define (i) hot plumes $P_{t,\mathrm{hot}}(r, \theta, z)$ where $q_t^c(r, \theta, z) \geqslant C\langle q_t^c \rangle_V$ and (ii) cold plumes $P_{t,\mathrm{cold}}(r, \theta, z)$ where $q_t^c(r, \theta, z) \leqslant -C\langle q_t^c \rangle_V$. Similarly, for angular velocity transport, we define (iii) hot (positive) plumes $P_{\omega,\mathrm{hot}}(r, \theta, z)$ where $q_\omega^c(r, \theta, z) \geqslant C\langle q_\omega^c \rangle_V$ and (iv) cold (negative) plumes $P_{\omega,\mathrm{cold}}(r, \theta, z)$ where $q_\omega^c(r, \theta, z) \leqslant -C\langle q_\omega^c \rangle_V$. The first subscript (t, ω) denotes heat and angular velocity, and the second subscript (hot, cold) denotes the hot and cold plumes, respectively.
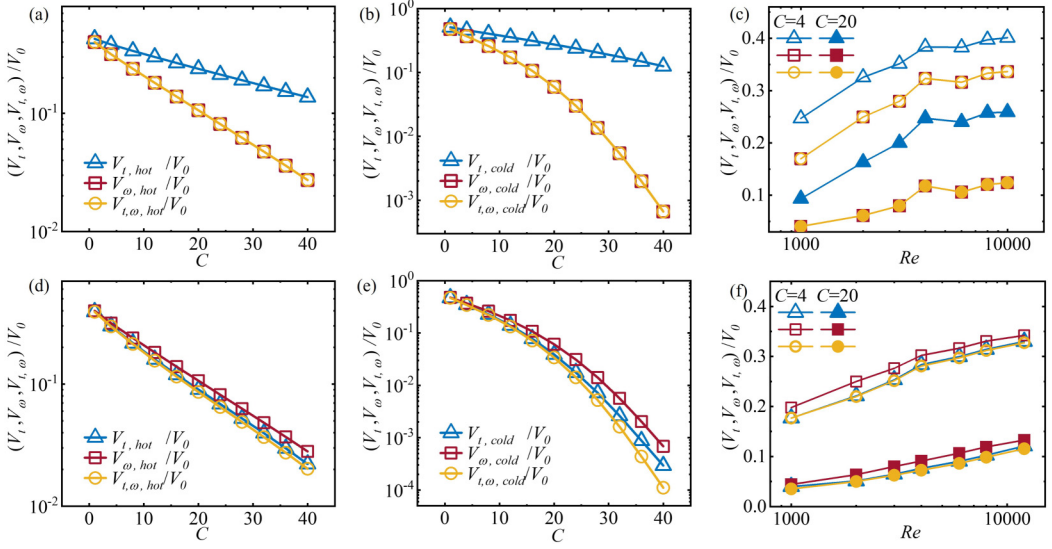
FIG. 6. Volume ratios of the hot (positive) (a), (d) and cold (negative) (b), (e) plumes for heat, angular velocity, and the mutual parts as functions of coefficient C for Re = 6000. (c), (f) Volume ratios of the hot (positive) plumes as functions of Re for various C. For all panels, we use Ra = 10^5. Results in panels (a)–(c) are for Pr = 4.38 and (d)–(f) are for Pr = 0.7.

The factor C is an empirical parameter chosen to be in the range of $1 \leqslant C \leqslant 40$ in this study. The mutual coherent structures are then defined as the overlapping volume of $P_t(r, \theta, z)$ and $P_\omega(r, \theta, z)$ as follows, (v) the mutual hot plumes $P_{t,\omega,\text{hot}}(r, \theta, z)$ where $q_t^c(r, \theta, z) \geqslant C\langle q_t^c \rangle_V$ and $q_\omega^c(r, \theta, z) \geqslant C\langle q_\omega^c \rangle_V$, and (vi) the mutual cold plumes $P_{t,\omega,\text{cold}}(r, \theta, z)$ where $q_t^c(r, \theta, z) \leqslant -C\langle q_t^c \rangle_V$ and $q_\omega^c(r, \theta, z) \leqslant -C\langle q_\omega^c \rangle_V$. Through time- and volume-averaging, we obtain the mean volumes of the hot plumes

$$V_{t,\text{hot}} = (V_0 \tau_0)^{-1} \int_{V,\tau} P_{t,\text{hot}} dV d\tau, \quad V_{\omega,\text{hot}} = (V_0 \tau_0)^{-1} \int_{V,\tau} P_{\omega,\text{hot}} dV d\tau, \quad (3)$$

the cold plumes

$$V_{t,\text{cold}} = (V_0 \tau_0)^{-1} \int_{V,\tau} P_{t,\text{cold}} dV d\tau, \quad V_{\omega,\text{cold}} = (V_0 \tau_0)^{-1} \int_{V,\tau} P_{\omega,\text{cold}} dV d\tau, \quad (4)$$

and the mutual plumes

$$V_{t,\omega,\text{hot}} = (V_0 \tau_0)^{-1} \int_{V,\tau} P_{t,\omega,\text{hot}} dV d\tau, \quad V_{t,\omega,\text{cold}} = (V_0 \tau_0)^{-1} \int_{V,\tau} P_{t,\omega,\text{cold}} dV d\tau, \quad (5)$$

where $V_0 = \int_V P dV$ and τ_0 denote the whole volume and time period.

The volume ratios V_t/V_0, V_ω/V_0 and $V_{t,\omega}/V_0$ for Pr = 4.38 are plotted as functions of C in Figs. 6(a) and 6(b). As shown in Fig. 6(a), these ratios for hot plumes are about 0.42 for $C = 1$, and decrease as C increases. Interestingly, data of the ratios $V_{\omega,\text{hot}}/V_0$ and $V_{t,\omega,\text{hot}}/V_0$ collapse, both decreasing more rapidly than $V_{t,\text{hot}}/V_0$. A similar trend is shown in Fig. 6(b) for the volume ratios of cold plumes. We see that the ratios of thermal plumes $V_{t,\text{hot}}/V_0$ and $V_{t,\text{cold}}/V_0$ are always greater than the angular velocity and the mutual ones, indicating a broader distribution of thermal structures. In Fig. 6(c), the volume ratios of hot (positive) plumes are plotted as functions of Re for two values of C. We see that with increasing Re, the ratios $V_{t,\text{hot}}/V_0$, $V_{\omega,\text{hot}}/V_0$ and $V_{t,\omega,\text{hot}}/V_0$ first increase and then the slopes become smaller when Re $\geqslant 4000$.

For the flows with low Pr = 0.7 [Figs. 6(d)–6(f)], the data show almost similar trends when the parameters C and Re change. We see that the volume ratios become greater when Re increases
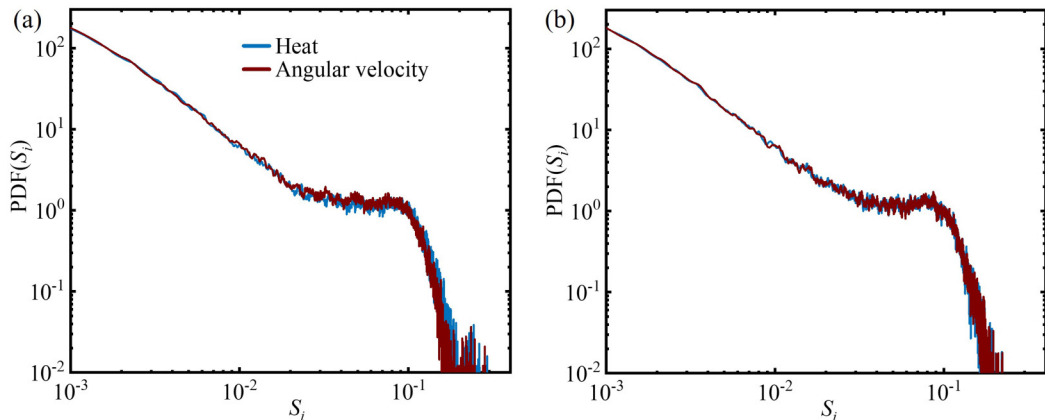
FIG. 7. Probability distribution functions of the area ratio S_i for $Pr = 4.38$ (a) and 0.7 (b), when $Re = 6000$ and $Ra = 10^5$. Here, $S_i = S(i)/S_0$ is defined as the area ratio of each plume in the meridional plane, where $S(i)$ denotes the ith plume's area that is identified by the C criteria and $S_0 = hd$ is the area of the meridional plane. To include more structures, we use a conventional value $C=1$ as the criteria, since a greater C corresponds to the smaller area with the higher density.

or when C decreases. However, here we find that V_ω/V_0 becomes slightly greater than V_t/V_0 and $V_{t,\omega}/V_0$ for low Pr. We attribute these to the Pr dependence of the flow properties, since heat is more likely to accumulate within the turbulent coherent structures for high $Pr = 4.38$ but becomes easier to diffuse for low $Pr = 0.7$. Results in Fig. 6 imply that in the high-Re regime, heat and angular momentum are transferred mainly through highly similar coherent structures. The flow regions of large angular momentum fluxes are nested within the regions of large heat fluxes for high $Pr = 4.38$ and vice versa for low $Pr = 0.7$.

To further reflect the distributions of the plumes' areas in the whole spatial and temporal domains, we show in Fig. 7 the probability distribution function of $S_i = S(i)/S_0$ in meridional planes. It is found that for each Pr, the plumes of heat and angular velocity have the same distributions all the time. We suggest that it is the similarities of the turbulent structures, which deliver efficiently both the heat and angular momentum transport, giving rise to the same scaling properties of Nu and ν_t/ν observed in Figs. 1–3.

IV. CONCLUDING REMARKS

We investigate numerically the heat and angular momentum transport processes in the turbulent TC flows which are subjected to a radial temperature gradient. A large range of Reynolds numbers is considered, extending the present study of the heat transport to the unexplored regime of turbulent TVs.

We find that the flows undergo a first transition at Re_1^* from the convection-dominated state in the form of a large-scale meridional circulation to the transitional regime typified by spiral vortices. After this transition, we observe enhanced transport of heat and angular momentum since rotations start to influence the flow structures. With increasing Re, the flow turns into the TC-dominated regime where the heat and angular momentum transport become independent of Ra. Eventually, the turbulent TVs start to dominate the turbulent transport processes at Re_2^*, after which the heat and angular momentum transport are dictated by power-law scalings, i.e., $Nu \sim Re^{0.619\pm0.015}$ for $Pr = 4.38$, $Nu \sim Re^{0.590\pm0.025}$ for $Pr = 0.7$ and $\nu_t/\nu \sim Re^{0.588\pm0.036}$ for both Pr. Our results also show that the transitional values Re_1^* and Re_2^* depend on both Ra and Pr.

From the point of view of Reynolds analogy, one can predict the momentum possesses similar transport behaviors as heat in turbulent flows [51]. However, an interesting finding here is the

existence of an analogous scaling law for radial transport of heat and angular momentum in turbulent TC flows. Besides their similar scaling exponents, our data show that the effective viscosity (ν_t/ν) and diffusivity (κ_t/κ) have almost the same efficiency for Re $>$ 2000. The similar properties of both types of transport are found to persist in the turbulent TV regime, which was attributed to the mutual structures through which heat and momentum are efficiently transported. Further analysis shows that the structures for high-efficiency angular momentum transport are nested inside the thermal ones for high Pr $=$ 4.38 or vice versa for low Pr $=$ 0.7. We note that the analogy between heat and momentum transport in rotating flow has been interpreted through the one-dimensional simplified model by Bradshaw [52]. To further connect the present results with Bradshaw's analogy is an intriguing subject for future studies. In addition, the similarity of TC, RB, and pipe flows has been found in Ref. [53]. The turbulent transport processes in these flows remain to be compared. In a TC system where an axial destabilized temperature gradient is applied, it has been reported that the axial heat transport has the same scaling as the radial angular momentum transport in the turbulent TV regime [33]. Hence, we suggest that it is the structures in forms of turbulent TVs that provide the TC systems with equal transport efficiencies in both the radial and axial directions. A direct application of the present study is to predict the global heat transfer based on the known driven torque and vice versa. Our results may be also applicable to understand the turbulent transport processes and the interior structures of stars, and to control the heat transport in industrial production processes of the TC-type reactors.

The ultimate regime of TC flows [54,55] sets in at a much larger Reynolds number (Re $> 6 \times 10^4$ for $\eta = 0.5$ [34,35,38]) than the parameters considered in the present paper. Whether a similar scaling of heat and angular momentum transport exists at higher Re and even in the ultimate regime remains a challenging problem for future studies.

APPENDIX A: NUMERICAL DETAILS

1. Grid sensitivity studies and main results

The results of the grid sensitivity studies are listed in Table II. It is shown that results of Nu and Re_τ show a good convergence as resolutions increase. The main results are listed in Tables III and IV. For all our runs, the smallest mean scales are, respectively, determined by the mean Kolmogrov scale $\langle\lambda_k\rangle_V = (\nu^3/\langle\epsilon_\nu\rangle_V)^{1/4}$ for Pr $=$ 0.7 and the mean Batchelor scale $\langle\lambda_b\rangle_V = (\kappa^2\nu/\langle\epsilon_\nu\rangle_V)^{1/4}$ for Pr $=$ 4.38, where $\langle\epsilon_\nu\rangle_V$ is the volume- and time-averaged turbulent kinetic energy dissipation rate [56–59]. At high Reynolds number, the flow enters into the shear-dominated regime that $\langle\lambda_b\rangle_V$ decreases rapidly with the increasing kinetic energy dissipation. Thus, the ratios of the greatest grid spacing $L_{\max}$ [60] to $\langle\lambda_k\rangle_V$ and $\langle\lambda_b\rangle_V$ [61] do not exceed 2.7 and 4.5, respectively, in this paper. Meanwhile, the minimal radial grid spacing in wall units is always less than unity. Besides

TABLE II. A summary of the grid sensitivities study for Ra $= 10^5$, Re $=$ 8000, and Pr $=$ 0.7.

$N_\theta(L_\theta) \times N_z \times N_r$	Nu	Re_τ	σ_{ϵ_T}	$L_{\max}/(\langle\lambda_k\rangle_V, \langle\lambda_b\rangle_V)$
$128(0.5\pi) \times 1025 \times 225$	13.54	232.95	0.02	2.45, 2.05
$192(0.5\pi) \times 1537 \times 225$	13.29	229.24	0.01	1.86, 1.56
$256(0.5\pi) \times 2049 \times 225$	13.20	229.53	0.01	1.51, 1.26

TABLE III. A summary of the main results for Pr = 4.38.

Re	Pr	Ra	$N_\theta(L_\theta) \times N_z \times N_r$	Nu	Re_τ	σ_{ϵ_T}	$L_{max}/(\langle\lambda_k\rangle_V, \langle\lambda_b\rangle_V)$	r_{min}^+, r_{max}^+
0	4.38	10^5	$128(2\pi) \times 257 \times 33$	3.27		0.00	0.90, 1.89	
25	4.38	10^5	$128(2\pi) \times 257 \times 33$	3.27	4.99	0.00	0.91, 1.91	0.07, 0.59
50	4.38	10^5	$128(2\pi) \times 257 \times 33$	3.27	7.06	0.00	0.94, 1.96	0.10, 0.84
70	4.38	10^5	$128(2\pi) \times 257 \times 33$	3.28	8.42	0.00	0.97, 2.02	0.12, 1.00
100	4.38	10^5	$128(2\pi) \times 257 \times 33$	3.32	10.16	0.00	1.02, 2.13	0.14, 1.20
150	4.38	10^5	$128(2\pi) \times 257 \times 33$	3.75	13.83	0.01	1.14, 2.39	0.19, 1.64
200	4.38	10^5	$128(2\pi) \times 321 \times 41$	4.22	16.64	0.01	1.27, 2.66	0.23, 1.72
300	4.38	10^5	$128(2\pi) \times 321 \times 41$	4.88	21.41	0.01	1.33, 2.79	0.23, 1.77
400	4.38	10^5	$128(2\pi) \times 321 \times 41$	5.37	25.29	0.02	1.54, 3.22	0.27, 2.40
500	4.38	10^5	$128(2\pi) \times 321 \times 41$	6.28	29.89	0.02	1.77, 3.69	0.32, 2.83
800	4.38	10^5	$128(2\pi) \times 385 \times 49$	7.70	40.88	0.02	2.05, 4.29	0.36, 3.23
1000	4.38	10^5	$192(2\pi) \times 513 \times 65$	8.43	47.74	0.02	1.76, 3.69	0.23, 3.09
1000	4.38	10^5	$64(0.5\pi) \times 513 \times 65$	8.47	47.89	0.02	1.60, 3.36	0.23, 3.10
2000	4.38	10^5	$256(2\pi) \times 721 \times 91$	11.63	77.46	0.03	1.93, 4.04	0.26, 3.57
2000	4.38	10^5	$96(0.5\pi) \times 721 \times 91$	11.74	77.65	0.03	1.69, 3.54	0.26, 3.58
3000	4.38	10^5	$128(0.5\pi) \times 897 \times 129$	14.98	105.63	0.04	1.64, 3.42	0.25, 3.42
4000	4.38	10^5	$128(0.5\pi) \times 1025 \times 161$	18.16	131.90	0.04	1.74, 3.65	0.25, 3.42
6000	4.38	10^5	$192(0.5\pi) \times 1281 \times 193$	23.19	183.50	0.04	1.73, 3.62	0.29, 3.96
8000	4.38	10^5	$256(0.5\pi) \times 1537 \times 225$	27.40	228.16	0.03	1.69, 3.53	0.30, 4.20
10000	4.38	10^5	$256(0.5\pi) \times 1793 \times 257$	31.90	275.04	0.04	1.77, 3.71	0.32, 4.46
15000	4.38	10^5	$256(0.5\pi) \times 2001 \times 301$	41.79	384.76	0.04	2.11, 4.43	0.38, 5.32
0	4.38	10^6	$256(2\pi) \times 513 \times 65$	5.75		0.00	0.93, 1.95	
25	4.38	10^6	$256(2\pi) \times 513 \times 65$	5.75	5.70	0.00	0.93, 1.95	0.04, 0.34
100	4.38	10^6	$256(2\pi) \times 513 \times 65$	5.75	11.42	0.00	0.94, 1.97	0.07, 0.68
200	4.38	10^6	$256(2\pi) \times 513 \times 65$	5.76	16.25	0.00	0.97, 2.03	0.11, 0.96
300	4.38	10^6	$256(2\pi) \times 513 \times 65$	6.21	21.93	0.00	1.01, 2.11	0.14, 1.30
500	4.38	10^6	$256(2\pi) \times 513 \times 65$	6.89	30.66	0.01	1.15, 2.42	0.20, 1.82
800	4.38	10^6	$256(2\pi) \times 513 \times 65$	7.92	41.98	0.02	1.46, 3.06	0.20, 2.72
1000	4.38	10^6	$256(2\pi) \times 513 \times 65$	8.67	48.69	0.03	1.64, 3.43	0.24, 3.15
1500	4.38	10^6	$256(2\pi) \times 641 \times 81$	10.37	63.72	0.03	1.77, 3.69	0.24, 3.25
2000	4.38	10^6	$384(2\pi) \times 721 \times 91$	11.75	77.97	0.02	1.69, 3.55	0.27, 3.59
4000	4.38	10^6	$128(0.5\pi) \times 1025 \times 161$	17.97	131.67	0.04	1.74, 3.65	0.25, 3.42
6000	4.38	10^6	$192(0.5\pi) \times 1281 \times 193$	23.38	181.11	0.04	1.72, 3.60	0.28, 3.90
8000	4.38	10^6	$256(0.5\pi) \times 1537 \times 225$	27.40	228.16	0.03	1.69, 3.53	0.30, 4.20

this, the relative error measurement σ_{ϵ_T} is employed to check the deviation of the exact balance between the thermal dissipation and the global heat transfer [58,59,62]. To reduce the computational requirements for high-Re flows, the azimuthal computational extents L_θ are reduced to a quarter of the cylinder (0.5π) for Re $\geqslant$ 4000. This strategy has been proven to be effective [63,64]. And, as shown in Tables III and IV, the simulations for $L_\theta = 2\pi$ and 0.5π are both performed in the range of $1000 \leqslant$ Re $\leqslant 4000$, and the results suggest that the shortened extents do not change the main results.

In Tables II–IV, $N_\theta \times N_z \times N_r$ denote the resolutions in three directions, and L_θ is the azimuthal computational extent; σ_{ϵ_T} is the relative error measured by Nu and the thermal dissipation rate; $\frac{L_{max}}{\langle\lambda_k\rangle_V, \langle\lambda_b\rangle_V}$ are the maximal grid spacings compared with the Kolmogrov and Batchelor scales; r_{min}^+, r_{max}^+ are the minimal and maximal grid sizes in wall units.

TABLE IV. A summary of the main results for Pr = 0.7.

Re	Pr	Ra	$N_\theta(L_\theta)\times N_z\times N_r$	Nu	Re_τ	σ_{ϵ_T}	$L_{\max}/(\langle\lambda_k\rangle_V, \langle\lambda_b\rangle_V)$	$r^+_{\min}, r^+_{\max}$
0	0.7	10^5	$128(2\pi) \times 257 \times 33$	3.17		0.00	2.36, 1.98	
50	0.7	10^5	$128(2\pi) \times 257 \times 33$	3.17	9.26	0.00	2.37, 1.99	0.10, 1.19
100	0.7	10^5	$128(2\pi) \times 257 \times 33$	3.17	13.06	0.00	2.38, 1.99	0.14, 1.69
200	0.7	10^5	$128(2\pi) \times 321 \times 41$	3.18	18.59	0.00	2.09, 1.75	0.15, 1.92
300	0.7	10^5	$128(2\pi) \times 321 \times 41$	3.19	22.83	0.00	2.15, 1.80	0.18, 2.36
400	0.7	10^5	$128(2\pi) \times 321 \times 41$	3.18	26.66	0.00	2.23, 1.86	0.22, 2.76
500	0.7	10^5	$128(2\pi) \times 321 \times 41$	3.33	30.87	0.01	2.30, 1.92	0.25, 3.19
800	0.7	10^5	$128(2\pi) \times 385 \times 49$	3.87	41.59	0.01	2.32, 1.94	0.28, 3.58
1000	0.7	10^5	$192(2\pi) \times 513 \times 65$	4.40	48.59	0.01	2.10, 1.76	0.23, 3.12
1000	0.7	10^5	$64(0.5\pi) \times 513 \times 65$	4.38	48.19	0.01	1.65, 1.38	0.23, 3.09
1500	0.7	10^5	$192(2\pi) \times 641 \times 81$	5.34	63.12	0.01	1.95, 1.63	0.24, 3.27
2000	0.7	10^5	$256(2\pi) \times 721 \times 91$	6.06	77.91	0.01	2.14, 1.79	0.27, 3.59
2000	0.7	10^5	$96(0.5\pi) \times 721 \times 91$	6.10	78.25	0.00	1.94, 1.63	0.27, 3.60
3000	0.7	10^5	$96(0.5\pi) \times 897 \times 113$	7.55	106.18	0.01	1.89, 1.58	0.29, 3.93
4000	0.7	10^5	$256(2\pi) \times 1025 \times 161$	8.70	132.14	0.01	2.20, 1.84	0.25, 3.43
4000	0.7	10^5	$128(0.5\pi) \times 1025 \times 161$	8.88	133.44	0.01	1.75, 1.47	0.25, 3.46
6000	0.7	10^5	$128(0.5\pi) \times 1281 \times 193$	11.20	182.83	0.01	1.98, 1.66	0.28, 3.95
8000	0.7	10^5	$192(0.5\pi) \times 1537 \times 225$	13.29	229.24	0.01	1.86, 1.56	0.31, 4.25
12 000	0.7	10^5	$192(0.5\pi) \times 1793 \times 257$	17.13	320.74	0.02	2.20, 1.84	0.37, 5.20
0	0.7	10^6	$256(2\pi) \times 513 \times 65$	5.49		0.00	2.41, 2.01	
50	0.7	10^6	$256(2\pi) \times 513 \times 65$	5.49	11.64	0.00	2.41, 2.00	0.06, 0.75
100	0.7	10^6	$256(2\pi) \times 513 \times 65$	5.48	16.47	0.00	2.41, 2.00	0.08, 0.89
200	0.7	10^6	$256(2\pi) \times 513 \times 65$	5.48	23.34	0.00	2.42, 2.03	0.11, 1.5
500	0.7	10^6	$256(2\pi) \times 513 \times 65$	5.48	37.44	0.00	2.45, 2.05	0.18, 2.40
800	0.7	10^6	$256(2\pi) \times 513 \times 65$	5.52	46.68	0.00	2.48, 2.07	0.23, 3.02
1000	0.7	10^6	$256(2\pi) \times 513 \times 65$	5.58	68.53	0.00	2.54, 2.13	0.26, 3.44
1500	0.7	10^6	$256(2\pi) \times 513 \times 65$	6.11	68.60	0.01	2.66, 2.22	0.33, 4.44
2000	0.7	10^6	$256(2\pi) \times 721 \times 91$	6.55	84.49	0.01	2.29, 1.92	0.29, 3.89
3000	0.7	10^6	$256(2\pi) \times 721 \times 91$	7.67	112.20	0.01	2.68, 2.24	0.38, 5.17
4000	0.7	10^6	$256(2\pi) \times 1025 \times 161$	8.84	133.96	0.02	1.89, 2.26	0.25, 3.47
6000	0.7	10^6	$128(0.5\pi) \times 1281 \times 193$	11.12	184.46	0.02	1.73, 3.62	0.29, 3.96

2. Discussions of the centrifugal buoyancy effects

In our system, the centrifugal buoyancy $F_{cb} = -(\beta\Delta)(U_\theta^2/R)T e_r$ [26,28] is present because of the azimuthal motion of the fluid. Here we perform the additional simulations for the experimental conditions with $\beta \approx 0.004\,\mathrm{K}^{-1}$ and $\Delta = 10\,\mathrm{K}$ for air and with $\beta \approx 0.00038\,\mathrm{K}^{-1}$ and $\Delta = 10\,\mathrm{K}$ for water. The results shown in Figs. 8(a) and 8(b) indicate that including the centrifugal buoyancy does not change the results of heat transport. Therefore, in this paper, the effect of centrifugal force is neglected.

3. Comparison with experimental results

To validate our results for the high-Re regime, we compare the heat-transport data with the previous experimental results in Fig. 8(a). Our results are consistent with the power-law scaling obtained in Ref. [65] for $2000 \leqslant \mathrm{Re} < 10\,000$. But for high Re > 10 000, it is found that Nu tends to deviate from the scaling law. We argue that the difference results from their fitting errors, since this scaling exponent is already same to the well-accepted value ($>2/3$) for ultimate turbulent regime [4].
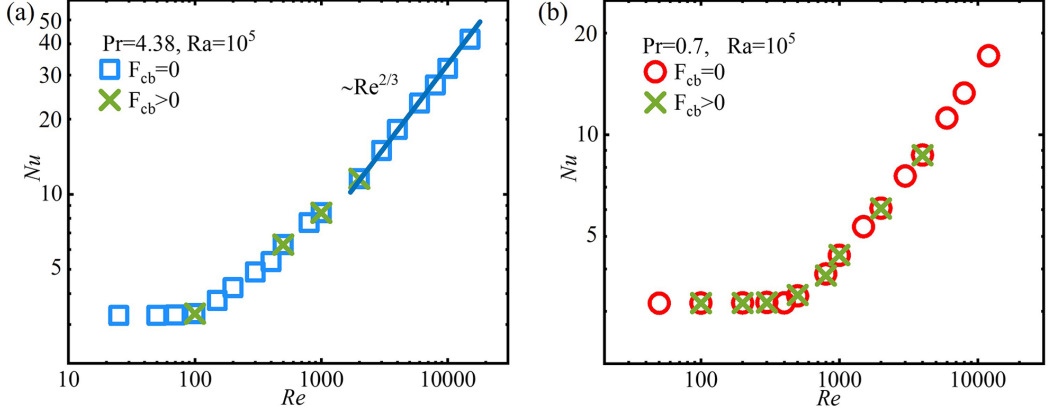
FIG. 8. Comparison of Nu as functions of Re when the centrifugal buoyancy is included ($F_{cb} > 0$) and excluded ($F_{cb} = 0$). Results for Pr = 4.38 (a), Pr = 0.7 (b) and Ra = 10^5. Solid line indicates the scaling law obtained from experiments [65].

APPENDIX B: DERIVATIONS OF FLUX DENSITIES, EFFECTIVE VISCOSITY AND DIFFUSIVITY

In our annular system, the ring surface increases as r increases, leading to a decreasing flux density along the radial direction. Hence, in this section the heat flux density q_t and the angular velocity flux density q_ω are defined, respectively, in addition to the common definitions of the heat and angular velocity currents.

1. Heat flux density q_t

Here we consider the dimensional fields of velocity $\mathbf{u}(r, \theta, z)$ and temperature $t(r, \theta, z)$. For a pure thermal conductive state between the concentric cylinders, the one-dimensional radial temperature distribution is $t(r) = c_1 \ln r + c_2$, with $c_1 = -\Delta/\ln(r_2/r_1)$ and $c_2 = t_2 - c_1 \ln(r_2)$. From Fourier's law, the radial heat flux density (by thermal conduction) is $q_t^{\mathrm{Lam}}(r) = -\kappa \partial_r t = -\kappa c_1/r$, which decreases along the radial direction owing to the enlarging ring surface. For the turbulent flow, the three-dimensional distributions of the heat flux density is defined as

$$q_t(r, \theta, z) = u_r(r, \theta, z)(t(r, \theta, z) - t_2) - \kappa \partial_r(t(r, \theta, z) - t_2), \tag{B1}$$

where the temperature of the cold wall t_2 is used as the reference temperature as done in Ref. [24]. The first term on the right-hand side corresponds to the convective contribution $q_t^c = u_r(r, \theta, z)(t(r, \theta, z) - t_2)$. Thus, the Nusselt number is defined as the ratio of the turbulent heat transport to the thermal conduction

$$\mathrm{Nu} = \frac{\langle q_t \rangle_V}{\langle q_t^{\mathrm{Lam}} \rangle_V} = a^{-1}(\mathrm{RePr}\langle U_r T \rangle_V - \partial_r \langle T \rangle_V), \tag{B2}$$

where $a = 2d^2/[\ln(r_2/r_1)(r_2^2 - r_1^2)]$ denotes the factor caused by the annular geometry.

2. Angular velocity flux density q_ω

In circular Couette flow (CCF), the flow is laminar and has purely azimuthal velocity $u_\theta = Ar + B/r$, with $A = (r_2 u_2 - r_1 u_1)/(r_2^2 - r_1^2)$ and $B = (r_2^2 r_1 u_1 - r_2 r_1^2 u_2)/(r_2^2 - r_1^2)$. Thus, its angular velocity flux density could be written as $q_\omega^{\mathrm{Lam}}(r) = 2\nu B/r$, which also decreases along the radial direction the same as q_t^{Lam}. Taking into account the increasing area in the radial direction, after multiplication with r, the conventional formula of the angular velocity current (for CCF) is

$J_\omega^{\mathrm{Lam}} = 2\nu B$ [40]. In turbulent flows, according to the derivations from Ref. [40], the conventional angular velocity current is expressed as

$$\langle J_\omega(r, \theta, z)\rangle_{\theta z} = r^2 \langle u_r(r, \theta, z)u_\theta(r, \theta, z)\rangle_{\theta z} - \nu r^3 \partial_r(\langle u_\theta(r, \theta, z)\rangle_{\theta z}/r). \tag{B3}$$

Here, without regard to the temporal and spatial averaging processes, the spatial distribution of J_ω is

$$J_\omega(r, \theta, z) = r^2 u_r(r, \theta, z)u_\theta(r, \theta, z) - \nu r^3 \partial_r(u_\theta(r, \theta, z)/r). \tag{B4}$$

When J_ω is divided by r, one could obtain the definition of angular velocity flux density:

$$q_\omega(r, \theta, z) = r u_r(r, \theta, z)u_\theta(r, \theta, z) - \nu r^2 \partial_r(u_\theta(r, \theta, z)/r). \tag{B5}$$

The convective part is $q_\omega^c = r u_r(r, \theta, z)u_\theta(r, \theta, z)$. It is worth noting that $\langle J_\omega\rangle_{\theta z}$ is the commonly conserved transverse current, whereas the density $\langle q_\omega\rangle_{\theta z}$ decreases along the radial direction the same as the heat flux density.

3. Effective viscosity ν_t/ν and diffusivity κ_t/κ

The global heat transfer could be defined as $Nu = Q_t/Q_t^{\mathrm{Lam}}$, where $Q_t = \int_{V,\tau} q_t dV d\tau$ and $Q_t^{\mathrm{Lam}} = \int_{V,\tau} q_t^{\mathrm{Lam}} dV d\tau$. To describe the contribution of turbulent transport to the global heat transfer, the effective thermal diffusivity κ_t is defined as $Q_t = \int_{V,\tau} \kappa_t(\Delta/d)dV d\tau$. Thus the dimensionless effective diffusivity is

$$\frac{\kappa_t}{\kappa} = a\mathrm{Nu}, \tag{B6}$$

where $a = 2d^2/[\ln(r_2/r_1)(r_2^2 - r_1^2)]$.

In the axially periodical domain or very long cylinders, $\langle J_\omega\rangle_{\theta z}$ remains constant radially. However, owing to the braking effect of the fixed end walls, $\langle J_\omega\rangle_{\theta z}$ decreases along the radial direction in our system. The angular velocity flux at the inner cylinder is [33],

$$\mathrm{Nu}_\omega = \frac{\langle J_\omega\rangle_{\theta z, r=r_1}}{J_\omega^{\mathrm{Lam}}} = \frac{u_1 d}{2B} \frac{(R_1^2)(2\mathrm{Re}_\tau)^2}{\mathrm{Re}}, \tag{B7}$$

where the friction Reynolds number Re_τ is defined as $\mathrm{Re}_\tau = 0.5u_\tau d/\nu$ with the friction velocity $u_\tau^2 = -\nu r(\partial_r\langle u_\theta/r\rangle_{\theta z})$ at the inner wall. Following Lathrop's estimation [31,32], we define the effective viscosity (owing to the turbulent transport) $\nu_t = G_{r_1}/(2\pi\rho u_1 r_1^2 h d^{-1})$, where the inner torque $G_{r_1} = 2\pi r_1^3 h\rho\nu\partial_r(\langle u_\theta/r\rangle_{\theta z}) = 2\pi r_1^2 h\rho\nu^2 d^{-2}(2\mathrm{Re}_\tau)^2$. Thus, one could obtain the equation of the dimensionless effective viscosity [33]:

$$\frac{\nu_t}{\nu} = \frac{(2\mathrm{Re}_\tau)^2}{\mathrm{Re}}. \tag{B8}$$

It is found that the dimensionless effective viscosity ν_t/ν and diffusivity κ_t/κ have the same scaling with the global transport of angular momentum (Nu_ω) and heat (Nu), respectively.

[1] A. K. M. F. Hussain, Coherent structures and turbulence, J. Fluid Mech. **173**, 303 (1986).

[2] T. L. Bergman, F. P. Incropera, D. P. DeWitt, and A. S. Lavine, *Fundamentals of Heat and Mass Transfer* (John Wiley & Sons, Hoboken, 2011)

[3] P. Holmes, J. L. Lumley, G. Berkooz, and C. W. Rowley, *Turbulence, Coherent Structures, Dynamical Systems and Symmetry*, 2nd ed., Cambridge Monographs on Mechanics (Cambridge University Press, Cambridge, 2012).

[4] S. Grossmann, D. Lohse, and C. Sun, High-Reynolds number Taylor-Couette turbulence, Annu. Rev. Fluid Mech. **48**, 53 (2016).

[5] G. Ahlers, S. Grossmann, and D. Lohse, Heat transfer and large scale dynamics in turbulent Rayleigh-Bénard convection, Rev. Mod. Phys. **81**, 503 (2009).

[6] M. A. Fardin, C. Perge, and N. Taberlet, "The hydrogen atom of fluid dynamics"—Introduction to the Taylor-Couette flow for soft matter scientists, Soft Matter **10**, 3523 (2014).

[7] H. T. Ji, M. Burin, E. Schartman, and J. Goodman, Hydrodynamic turbulence cannot transport angular momentum effectively in astrophysical disks, Nature (London) **444**, 343 (2006).

[8] H. Ji and S. Balbus, Angular momentum transport in astrophysics and in the lab, Phys. Today **66**(8), 27 (2013).

[9] M. Avila, Stability and Angular-Momentum Transport of Fluid Flows Between Corotating Cylinders, Phys. Rev. Lett. **108**, 124501 (2012).

[10] T. H. van den Berg, S. Luther, D. P. Lathrop, and D. Lohse, Drag Reduction in Bubbly Taylor-Couette Turbulence, Phys. Rev. Lett. **94**, 044501 (2005).

[11] D. P. M. van Gils, D. Narezo Guzman, C. Sun, and D. Lohse, The importance of bubble deformability for strong drag reduction in bubbly turbulent Taylor–Couette flow, J. Fluid Mech. **722**, 317 (2013).

[12] C. Vives, Effects of a forced couette flow during the controlled solidification of a pure metal, Int. J. Heat Mass Transf. **31**, 2047 (1988).

[13] G. B. McFadden, S. R. Coriell, B. T. Murray, M. E. Glicksman, and M. E. Selleck, Effect of a crystal–melt interface on Taylor-vortex flow, Phys. Fluids **2**, 700 (1990).

[14] K. Kataoka, N. Ohmura, M. Kouzu, Y. Simamura, and M. Okubo, Emulsion polymerization of styrene in a continuous Taylor vortex flow reactor, Chem. Eng. Sci. **50**, 1409 (1995).

[15] B. Haut, H. B. Amor, L. Coulon, A. Jacquet, and V. Halloin, Hydrodynamics and mass transfer in a Couette–Taylor bioreactor for the culture of animal cells, Chem. Eng. Sci. **58**, 777 (2003).

[16] H. Masuda, T. Horie, R. Hubacz, N. Ohmura, and M. Shimoyamada, Process development of starch hydrolysis using mixing characteristics of Taylor vortices, Biosci. Biotechnol. Biochem. **81**, 755 (2017).

[17] H. A. Snyder and S. K. F. Karlsson, Experiments on the stability of Couette motion with a radial thermal gradient, Phys. Fluids **7**, 1696 (1964).

[18] M. M. Sorour and J. E. R. Coney, The effect of temperature gradient on the stability of flow between vertical, concentric, rotating cylinders, J. Mech. Eng. Sci. **21**, 403 (1979).

[19] K. S. Ball, B. Farouk, and V. C. Dixit, An experimental study of heat transfer in a vertical annulus with a rotating inner cylinder, Int. J. Heat Mass Transf. **32**, 1517 (1989).

[20] V. Lepiller, A. Goharzadeh, A. Prigent, and I. Mutabazi, Weak temperature gradient effect on the stability of the circular Couette flow, Eur. Phys. J. B **61**, 445 (2008).

[21] H. Singh, A. Bonnesoeur, H. Besnard, C. Houssin, A. Prigent, O. Crumeyrolle, and I. Mutabazi, A large thermal turbulent Taylor-Couette (THETACO) facility for investigation of turbulence induced by simultaneous action of rotation and radial temperature gradient, Rev. Sci. Instrum. **90**, 115112 (2019).

[22] J. Wen, W.-Y. Zhang, L.-Z. Ren, L.-Y. Bao, D. Dini, H. D. Xi, and H. B. Hu, Controlling the number of vortices and torque in Taylor–Couette flow, J. Fluid Mech. **901**, A30 (2020).

[23] M. Ali and P. D. Weidman, On the stability of circular Couette flow with radial heating, J. Fluid Mech. **220**, 53 (1990).

[24] C. Kang, K. S. Yang, and I. Mutabazi, Thermal effect on large-aspect-ratio Couette–Taylor system: Numerical simulations, J. Fluid Mech. **771**, 57 (2015).

[25] O. N. Kirillov and I. Mutabazi, Short-wavelength local instabilities of a circular Couette flow with radial temperature gradient, J. Fluid Mech. **818**, 319 (2017).

[26] H. N. Yoshikawa, M. Nagata, and I. Mutabazi, Instability of the vertical annular flow with a radial heating and rotating inner cylinder, Phys. Fluids **25**, 114104 (2013).

[27] R. Kedia, M. L. Hunt, and T. Colonius, Numerical simulations of heat transfer in Taylor-Couette flow, J. Heat Transfer **120**, 65 (1998).

[28] R. Guillerm, C. Kang, C. Savaro, V. Lepiller, A. Prigent, K. S. Yang, and I. Mutabazi, Flow regimes in a vertical Taylor-Couette system with a radial thermal gradient, Phys. Fluids **27**, 094101 (2015).

[29] H. Teng, N. Liu, X. Lu, and B. Khomami, Direct numerical simulation of Taylor-Couette flow subjected to a radial temperature gradient, Phys. Fluids **27**, 125101 (2015).

[30] C. Kang, A. Meyer, I. Mutabazi, and H. N. Yoshikawa, Radial buoyancy effects on momentum and heat transfer in a circular Couette flow, Phys. Rev. Fluids **2**, 053901 (2017).

[31] D. P. Lathrop, J. Fineberg, and H. L. Swinney, Transition to shear-driven turbulence in Couette–Taylor flow, Phys. Rev. A **46**, 6390 (1992).

[32] D. P. Lathrop, J. Fineberg, and H. L. Swinney, Turbulent Flow Between Concentric Rotating Cylinders at Large Reynolds Number, Phys. Rev. Lett. **68**, 1515 (1992).

[33] X. Y. Leng, D. Krasnov, B. W. Li, and J. Q. Zhong, Flow structures and heat transport in Taylor–Couette systems with axial temperature gradient, J. Fluid Mech. **920**, A42 (2021).

[34] R. Ostilla-Mónico, E. P. Van Der Poel, R. Verzicco, S. Grossmann, and D. Lohse, Exploring the phase diagram of fully turbulent Taylor–Couette flow, J. Fluid Mech. **761**, 1 (2014).

[35] R. C. A. van der Veen, S. G. Huisman, S. Merbold, U. Harlander, C. Egbers, D. Lohse, and C. Sun, Taylor–Couette turbulence at radius ratio $\eta = 0.5$: Scaling, flow structures and plumes, J. Fluid Mech. **799**, 334 (2016).

[36] A. Froitzheim, S. Merbold, R. Ostilla-Mónico, and C. Egbers, Angular momentum transport and flow organization in Taylor-Couette flow at radius ratio of $\eta =0.357$, Phys. Rev. Fluids **4**, 084605 (2019).

[37] S. Dong, Direct numerical simulation of turbulent Taylor–Couette flow, J. Fluid Mech. **587**, 373 (2007).

[38] S. Merbold, H. J. Brauckmann, and C. Egbers, Torque measurements and numerical determination in differentially rotating wide gap Taylor-Couette flow, Phys. Rev. E **87**, 023014 (2013).

[39] S. Grossmann and D. Lohse, Scaling in thermal convection: A unifying theory, J. Fluid Mech. **407**, 27 (2000).

[40] B. Eckhardt, S. Grossmann, and D. Lohse, Torque scaling in turbulent Taylor–Couette flow between independently rotating cylinders, J. Fluid Mech. **581**, 221 (2007).

[41] D. Krasnov, O. Zikanov, and T. Boeck, Comparative study of finite difference approaches in simulation of magnetohydrodynamic turbulence at low magnetic Reynolds number, Comput. Fluids **50**, 46 (2011).

[42] X. Y. Leng, Y. B. Kolesnikov, D. Krasnov, and B. W. Li, Numerical simulation of turbulent Taylor–Couette flow between conducting cylinders in an axial magnetic field at low magnetic Reynolds number, Phys. Fluids **30**, 015107 (2018).

[43] R. Akhmedagaev, O. Zikanov, D. Krasnov, and J. Schumacher, Turbulent Rayleigh–Bénard convection in a strong vertical magnetic field, J. Fluid Mech. **895**, R4 (2020).

[44] J. C. Adams, P. Swarztrauber, and R. Sweet, Efficient fortran subprograms for the solution of separable elliptic partial differential equations, https://www2.cisl.ucar.edu/resources/legacy/fishpack/.

[45] O. Shishkina, Momentum and heat transport scalings in laminar vertical convection, Phys. Rev. E **93**, 051102(R) (2016).

[46] L. Soucasse, P. Rivire, A. Soufiani, S. Xin, and P. Le Qur, Transitional regimes of natural convection in a differentially heated cubical cavity under the effects of wall and molecular gas radiation, Phys. Fluids **26**, 024105 (2014).

[47] G. E. Lau, G. H. Yeoh, V. Timchenko, and J. A. Reizes, Large-eddy simulation of turbulent buoyancy-driven flow in a rectangular cavity, Int. J. Heat Fluid Flow **39**, 28 (2013).

[48] D. C. Kuo and K. S. Ball, Taylor–Couette flow with buoyancy: Onset of spiral flow, Phys. Fluids **9**, 2872 (1997).

[49] O. Shishkina and C. Wagner, Local heat fluxes in turbulent Rayleigh-Bénard convection, Phys. Fluids **19**, 085107 (2007).

[50] S.-D. Huang, M. Kaczorowski, R. Ni, and K.-Q. Xia, Confinement-Induced Heat-Transport Enhancement in Turbulent Thermal Convection, Phys. Rev. Lett. **111**, 104501 (2013).

[51] W. M. Kays and M. E. Crawford, *Convective Heat and Mass Transfer* (McGraw-Hill, New York, 1993).

[52] P. Bradshaw, The analogy between streamline curvature and buoyancy in turbulent shear flow, J. Fluid Mech. **36**, 177 (1969).

[53] B. Eckhardt, S. Grossmann, and D. Lohse, What Rayleigh-Bénard, Taylor-Couette and pipe flows have in common, in *Progress in Turbulence II* (Springer, Berlin, 2007), pp. 3–10.

[54] S. G. Huisman, D. P. M. van Gils, S. Grossmann, C. Sun, and D. Lohse, Ultimate Turbulent Taylor-Couette Flow, Phys. Rev. Lett. **108**, 024501 (2012).

[55] X. Zhu, R. A. Verschoof, D. Bakhuis, S. G. Huisman, R. Verzicco, C. Sun, and D. Lohse, Wall roughness induces asymptotic ultimate turbulence, Nat. Phys. **14**, 417 (2018).

[56] G. K. Batchelor, Small-scale variation of convected quantities like temperature in turbulent fluid. Part 1. General discussion and the case of small conductivity, J. Fluid Mech. **5**, 113 (1959).

[57] S. B. Pope, *Turbulent Flows* (Cambridge University Press, Cambridge, 2000).

[58] R. J. A. M. Stevens, R. Verzicco, and D. Lohse, Radial boundary layer structure and nusselt number in Rayleigh-Bénard convection, J. Fluid Mech. **643**, 495 (2010).

[59] J. D. Scheel, M. S. Emran, and J. Schumacher, Resolving the fine-scale structure in turbulent Rayleigh-Bénard convection, New J. Phys. **15**, 113063 (2013).

[60] M. S. Emran and J. Schumacher, Fine-scale statistics of temperature and its derivatives in convective turbulence, J. Fluid Mech. **611**, 13 (2008).

[61] G. Grötzbach, Spatial resolution requirements for direct numerical simulation of the Rayleigh-Bénard convection, J. Comput. Phys. **49**, 241 (1983).

[62] B. I. Shraiman and E. D. Siggia, Heat transport in high-Rayleigh-number convection, Phys. Rev. A **42**, 3650 (1990).

[63] H. J. Brauckmann and B. Eckhardt, Direct numerical simulations of local and global torque in Taylor–Couette flow up to Re = 30000, J. Fluid Mech. **718**, 398 (2013).

[64] R. Ostilla-Mónico, R. Verzicco, and D. Lohse, Effects of the computational domain size on direct numerical simulations of Taylor-Couette turbulence with stationary outer cylinder, Phys. Fluids **27**, 025110 (2015).

[65] F. Tachibana and S. Fukui, Convective heat transfer of the rotational and axial flow between two concentric cylinders, Bull. JSME **7**, 385 (1964).